ELSEVIER

Earth and Planetary Science Letters 172 (1999) 23–37

EPSL

www.elsevier.com/locate/epsl

Source parameters of the 1 October 1995 Dinar (Turkey) earthquake from SAR interferometry and seismic bodywave modelling

T.J. Wright [a,*], B.E. Parsons [a], J.A. Jackson [b], M. Haynes [c], E.J. Fielding [a,1], P.C. England [a], P.J. Clarke [a,2]

[a] *Department of Earth Sciences, University of Oxford, Parks Rd, Oxford, OX1 3PR, UK*
[b] *Department of Earth Sciences, University of Cambridge, Downing Street, Cambridge, UK*
[c] *Nigel Press Associates, Crockham Park, Edenbridge, Kent, TN8 6SR, UK*

Received 6 January 1998; accepted 29 July 1999

Abstract

The 1 October 1995, $M_s = 6.1$ Dinar earthquake ruptured a 10 km section of the NW–SE Dinar–Çivril fault. There are discrepancies between the published source parameters from seismic data, with seismic moments in disagreement by over a factor of two. We use both SAR interferometry and seismic bodywave modelling to determine earthquake source parameters. An interferogram generated from ERS-1/2 SAR imagery spanning the event, and separated by 5 months, is used to derive source parameters by a downhill simplex inversion with multiple Monte-Carlo restarts. We model the displacements in the satellite line of sight, initially using uniform slip on a rectangular dislocation in an elastic half-space. The resultant model fault plane agrees in strike and location with the observed surface break, but systematic residuals exist in the line-of-sight deformation field, resulting in a r.m.s. residual of 20 mm in the interferogram. The residuals are reduced if the depth distribution of slip is allowed to vary spatially in four segments along a continuous fault plane. Our best-fitting solution, with a r.m.s. misfit of 8 mm, reveals two distinct areas of slip on the fault plane (strike 145º, dip 49º, rake 270º): a main rupture slipping by 1.44 m between depths of 1 and 8 km, becoming deeper to the SE and matching the observed surface rupture, and an along-strike continuation to the NW of the same fault plane, but between depths of 8 and 13 km and not associated with a surface break. The total geodetic moment ($4.5 \pm 0.1 \times 10^{18}$ N m) is more than twice as large as published seismic moments based on the inversion of P-waveforms alone, but close to the Harvard CMT moment (4.7×10^{18} N m). We use SH-waveforms, in addition to the P-waves used previously, to determine an alternative seismic source mechanism. SH-waves constrain the depth to be shallower than solutions based on P-waves alone, agreeing with the depths from the interferometric inversion and resulting in a larger moment ($3.1 \pm 0.4 \times 10^{18}$ N m) than the previous bodywave estimates ($2, 2.1 \times 10^{18}$ N m). The CMT moment reduces in magnitude to a similar size (3.3×10^{18} N m) if the centroid depth and fault dip are constrained to the values determined from bodywave modelling and interferometry. Thus, the geodetic moment is 40% bigger than the moment determined from seismology.

Keywords: earthquakes; SAR; interferometry; seismic migration; body waves; models

* Corresponding author. Tel.: +44 1865 272016; E-mail: tim.wright@earth.ox.ac.uk
[1] Also at Jet Propulsion Laboratory, 4800 Oak Grove Drive, Pasadena, CA, 91109, USA.
[2] Now at Department of Geomatics, University of Newcastle, Newcastle, NE1 7RU, UK.

0012-821X/99/$ – see front matter
PII: S0012-821X(99)00186-7

1. Introduction

Southwest Turkey forms part of the highly seismically active Aegean extensional domain [1,2], characterised by distributed N–S extension (Fig. 1). GPS crustal velocity measurements [3] indicate a regional extension rate of 14 ± 5 mm yr^{-1}. In southwest Anatolia the tectonic setting is more complex, with the Isparta Angle representing the intersection of the Hellenic and Cyprus arcs [4]. Both NE–SW- and NW–SE-striking faults are present, with the former appearing to be the dominant system. The NE–SW Fethiye–Burdur fault zone, characterised by normal faulting with an element of left-lateral slip [5,6], is the northeastern extension of the Pliny–Strabo fault zone (part of the Hellenic arc) and has been the site of a number of large earthquakes this century. At its northeastern end, the Fethiye–Burdur fault zone is limited by a NW–SE-striking fault, the Dinar–Çivril fault.

The 1 October 1995, $M_s = 6.1$, Dinar earthquake ruptured a section of the Dinar–Çivril fault causing extensive damage to the town of Dinar and killing 92 inhabitants. The fault is characterised by a 60

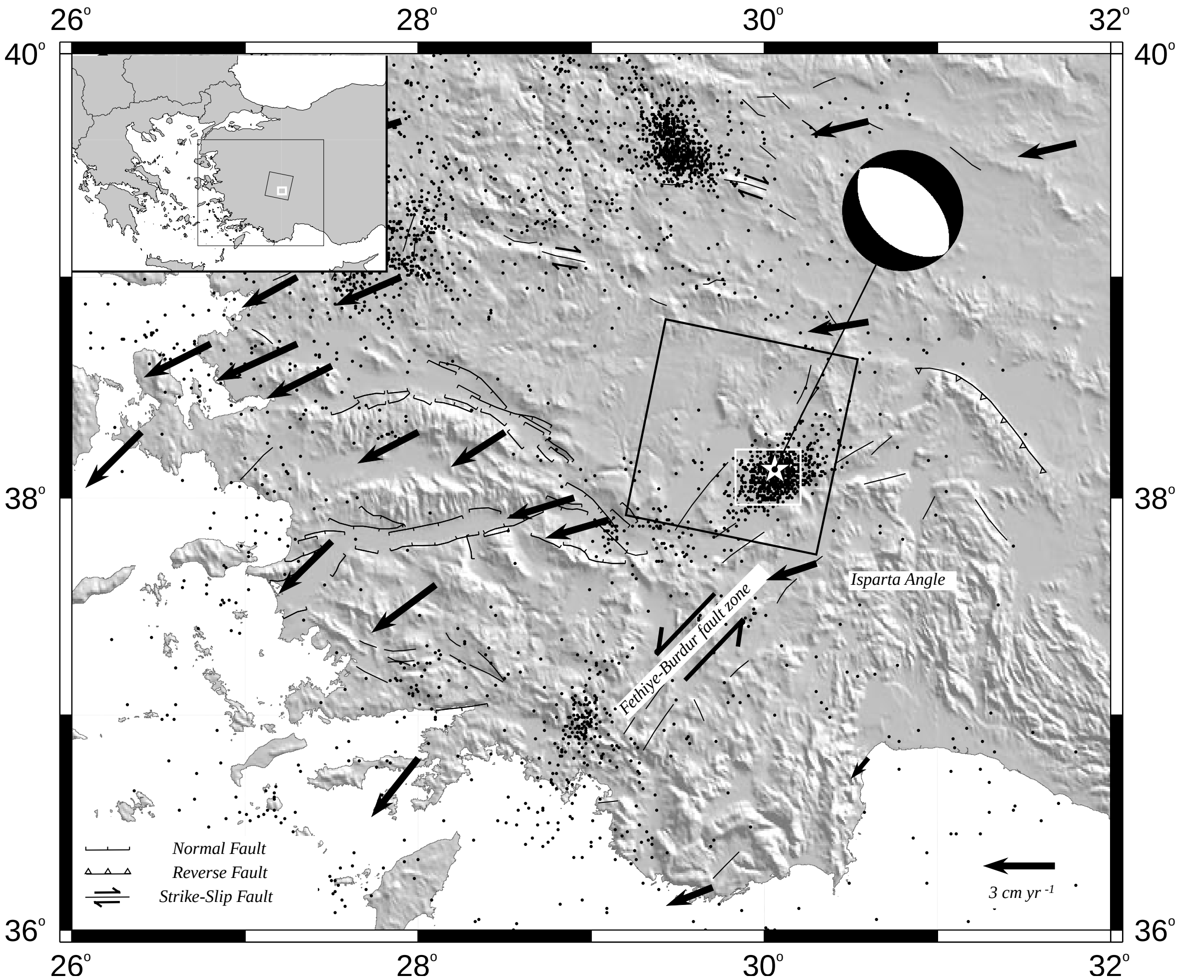

Fig. 1. Location of the 1 October 1995 Dinar earthquake with focal mechanism derived from inversion of P- and SH-waveforms (this study) superimposed on a regional shaded relief map generated from the GLOBE 1 km topography database [http://www.ngdc.noaa.gov/seg/topo/globe.shtml]. The nominal footprint of the ERS SAR scene used (inclined black box), and the extents of the sub-scene displayed in Figs. 3–6 (white box), are also shown, along with the major faults of the region [7] and all recorded seismic activity from the ISC catalogue for January 1995–March 1996. Arrows indicate GPS velocities relative to Eurasia [3].

Table 1
Source parameters of the 1 October 1995 Dinar Earthquake from seismology

	Lat., Long. [a]	M_0/N_M	Strike	Dip	Rake	Depth
Harvard CMT catalogue	38.06º, 29.68º	4.7×10^{18}	125º	30º	267º	15 km [b]
CMT (adjusted dip) [d]	38.06º, 29.68º	4.1×10^{18}	125º	45º	267º	15 km [b]
CMT (adjusted depth) [e]	38.06º, 29.68º	3.3×10^{18}	136º	45º	270º	4 km
Eyidǒgan and Barka [8]						
1st sub-event	38.10º, 30.175º	0.38×10^{18}	135º (fixed)	40º	255º	8 km
2nd sub-event		1.64×10^{18}	135º (fixed)	62º	221º	12 km
Pinar [15]						
1st sub-event	38.09º, 30.15º	0.5×10^{18}	121º	34º	261º	10 km
2nd sub-event		1.6×10^{18}	137º	40º	277º	15 km
This study [f]	38.06º, 30.13º	3.1×10^{18}	136º	43º	273º	4 km

[a] Epicentral location.
[b] This depth was held fixed in the HRV CMT inversion.
[c] 60 stations used in HRV inversion with 141 components (P, SH, SV).
[d] M_{xz} and M_{yz} components of the moment tensor set to zero (dip of 45º) (G. Ekström, pers. commun.).
[e] As above except that depth is fixed to 7 km in PREM (4 km into solid earth) (G. Ekström, pers. commun.).
[f] From P- and SH-waveform modelling. This solution used 42 waveforms (21 P-waves, 21 SH-waves) compared to the 10 and 16 waveforms (P-waves only) used by Eyidǒgan and Barka [8] and Pinar [15], respectively.

km scarp with up to 1500 m of relief to the NE, although there is only approximately half this relief at the rupture location. The earthquake created a 10 km continuous surface rupture running along the base of the scarp with a maximum vertical offset of 25–30 cm, tailing off to around 15 cm to the SE [8]. Landsat TM imagery is used in conjunction with a digital elevation model derived in this study to give a perspective view of the Dinar–Çivril fault (Fig. 2). The topography has a classic tilted block geometry with a steep scarp against the fault plane and gently tilted backslope.

There are differences between published seismic source parameters (Table 1), with seismic moments in disagreement by over a factor of two. The scaling of seismic moment, M_0, with fault length and width is fundamentally important in seismology and has been studied by many authors, e.g. [9,10]. Accurate knowledge of moment release is also vital for seismic hazard analysis [11] and for determining regional strain rates [12–14]. In this study we use Synthetic Aperture Radar (SAR) interferometry to determine fault length, width, and slip separately and hence M_0 independently of seismology. Our geodetic solution for the source parameters of the Dinar earthquake constrains the seismic moment to be larger than previous solutions based on P-wave modelling [8,15] but close to the Harvard CMT solution [16]. However, uncertainties in the determination of the M_{xz} and M_{yz} components of the moment tensor for shallow events [18,19], and the use of a fixed centroid depth, result in uncertainties in the CMT estimate of scalar moment. We further constrain the seismic solution using source parameters determined by joint inversion of SH- and P-waveforms; in particular, we investigate the possibility of subevents with different source mechanisms [8,15], and place better constraints on the M_{xz} and M_{yz} components of the moment tensor, and on the depth of faulting, than can be obtained with CMT solutions.

2. SAR interferometry

Studies of previous earthquakes, the 1992 Landers, California event in particular, have established SAR interferometry as a valuable technique for studying ground displacements caused by earthquakes [20–25]. The phase information from SAR images of the ground surface, acquired before and after an event in which ground displacements have occurred, can be used to generate an interferogram giving measurements of line-of-sight ground displacements with subcentimetric precision over a

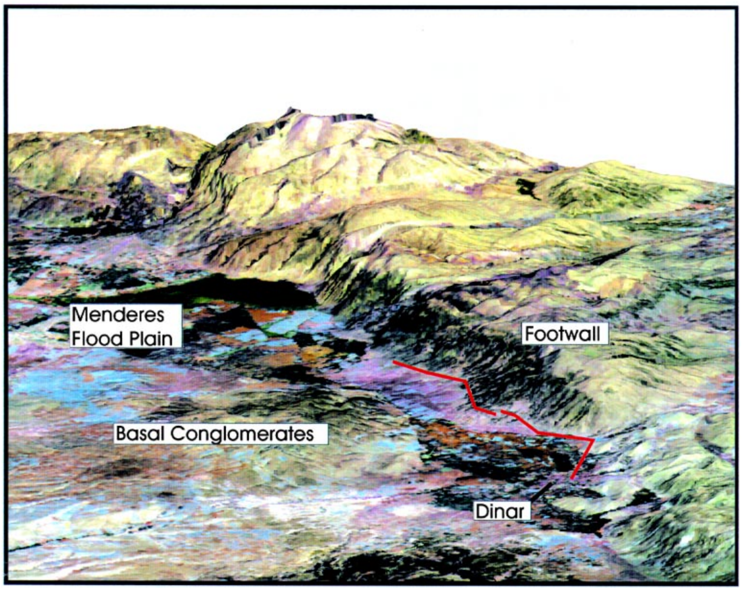

Fig. 2. Simulated 3D view looking NE along the Dinar fault, generated by draping Landsat TM data (bands 753 as rgb) over the high resolution DEM of the area generated in this study. The trace of the mapped surface rupture (red line) and the location of Dinar are shown [8]. Coherence in the interferogram is strongly correlated with surface type with high coherence over the basal conglomerates but low coherence over the agricultural flood plain of the Menederes river.

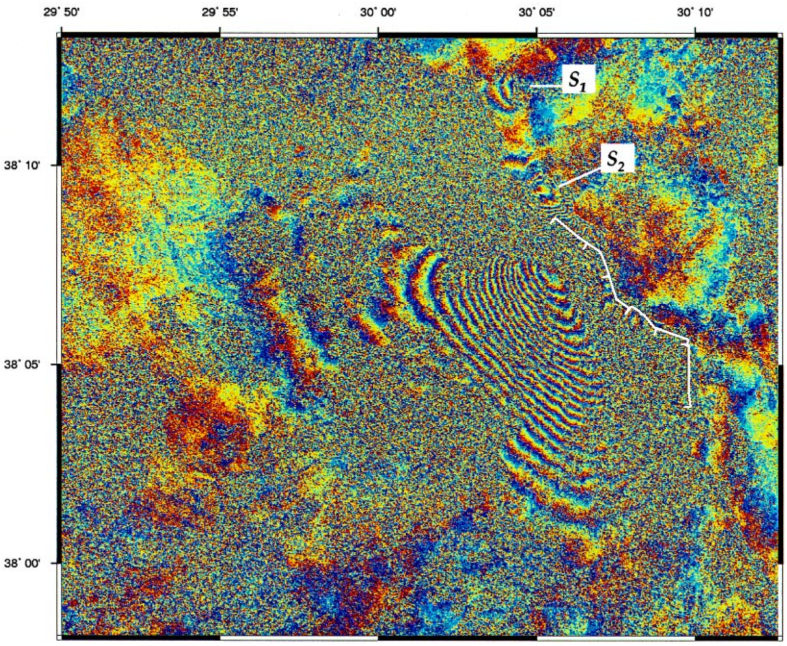

Fig. 3. Interferogram for the Dinar earthquake showing the location of the surface rupture (white line). The interferogram has been corrected for topographic contribution using a DEM derived from a SAR tandem pair. S_1 and S_2 denote the location of localised, high-gradient residual fringes, probably the result of small shallow aftershocks, or landslips.

Table 2
Details of ERS data used in this study (all SAR data copyright ESA)

	Date 1	Orbit 1	Date 2	Orbit 2	$B_\perp$ [a]	h_a [a]
(A) Change detection	13/08/95	21323 (ERS-1) [b]	01/01/96	3654 (ERS-2) [b]	8 m	1165 m
(B) DEM generation	22/10/95	2652 (ERS-2) [b]	23/10/95	22325 (ERS-1) [b]	116 m	81 m

[a] $B_\perp$ is the perpendicular baseline separation of the satellite orbits at the scene centre; $h_a \simeq 9416/B_\perp$. There is minimal along-track variation in $B_\perp$ for these data.
[b] Track 293, frame 2835.

wide area with a high spatial sampling rate; each fringe in the interferogram corresponds to 28 mm of ground displacement in the satellite line of sight for ERS-1/2.

Coseismic movements from the Dinar earthquake are measured using ERS SAR images spanning the event (Table 2, pair A) with a 5-month temporal separation and a 1165 m altitude of ambiguity (h_a) at the scene centre; i.e. topographic relief of 1165 m produces one fringe in the interferogram. We use the PulSAR SAR processing software, supported by Phoenix Systems, and the DERAin interferometric software, developed by the UK Defence Evaluation and Research Agency, to create the coseismic interferogram. The orbital parameters are updated using precise orbits from the German Processing and Archiving Facility for ERS (D-PAF).

The small topographic contribution to the net fringes is removed using a high resolution Digital Elevation Model (DEM, Fig. 2) constructed from an ERS tandem pair (Table 2, pair B), using the ROI_pac software at JPL. The unwrapped phase differences [26] are converted to elevations [27] with the effective baseline and phase constant being determined by comparing the unwrapped phase with a medium resolution DEM for the Dinar area.

The corrected coseismic interferogram (Fig. 3) shows 21 fringes in the hanging wall of the fault indicating a maximum line-of-sight downthrown displacement of 0.59 m. The hanging-wall fringe pattern indicates asymmetrical deformation with the maximum change in range towards the NW end of the observed surface rupture but about 2 km away from it, forming a 'bull's eye' pattern. At greater distances from the surface rupture, fringes run subparallel to the strike direction, widening to the NW before curving sharply inwards towards the ground break. Three upthrown fringes (85 mm) appear in the footwall of the fault after the topographic correction. Coherence in the interferogram is strongly correlated with surface cover, showing high coherence over the basal conglomerates in the footwall but low coherence over the agricultural flood plain of the Menederes river.

In addition to the fringes resulting directly from the earthquake there are two localised high-gradient fringe patterns (S_1, S_2). S_1 lies on the steep mountainside and S_2 lies at the base of the slope on alluvial fan deposits. Possible causes for these localised displacements include secondary faulting and landslips triggered by the earthquake. The features, a maximum of 2 km across, are too small to be a significant part of the main rupture.

3. Interferometric determination of source parameters

We digitise discrete line-of-sight displacements at 753 locations along identifiable fringe boundaries (where phase $= 0$ or 2π; Fig. 4). The line-of-sight displacement at each point is determined relative to a nominally zero-displacement outer fringe, away from the influence of the earthquake. Initially, the event is modelled by assuming the surface deformation is equivalent to that caused by uniform slip on a single rectangular dislocation in an elastic half-space [28], assuming Lamé elastic constants $\lambda = 3.22 \times 10^{10}$ Pa and $\mu = 3.43 \times 10^{10}$ Pa. The calculated surface displacement vector ($\boldsymbol{u}$) is projected into a line-of-sight displacement ($\Delta l = \hat{\boldsymbol{n}} \cdot \boldsymbol{u}$) where $\hat{\boldsymbol{n}}$ is the unit vector in the line of sight; (east, north, up) $= (0.3523, -0.0768, 0.9327)$.

We adopt a hybrid Monte-Carlo, downhill simplex inversion technique [29,30] to calculate a best-fitting model to the fringe pattern. The downhill simplex

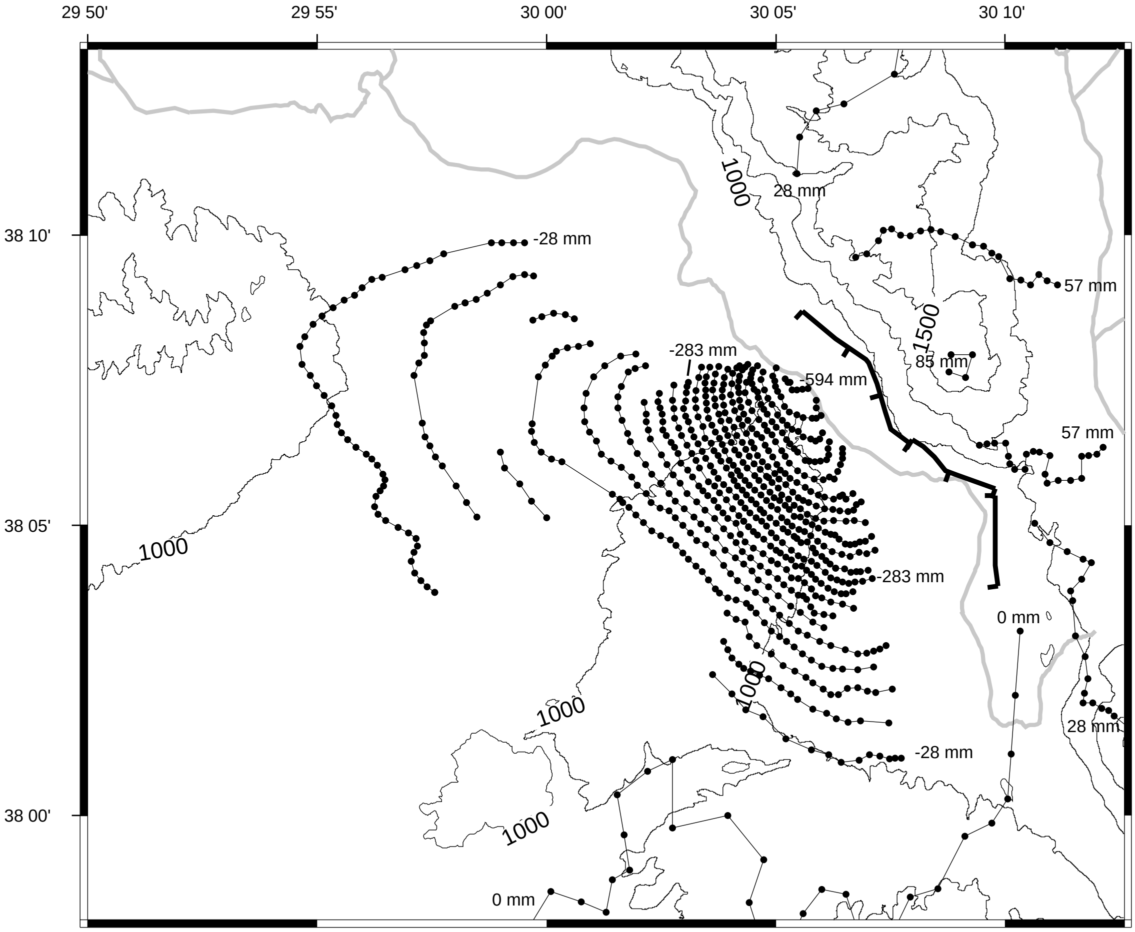

Fig. 4. Location of digitised fringe boundaries, where phase $= 0$ or 2π, used to constrain interferometric inversion. Discrete points are represented by dots with black lines joining points of equal phase. Line-of-sight displacements are measured relative to the outer fringe. Also shown are topographic contours at 250 m intervals from the digital elevation model derived in this study, the location of the Menderes river (grey line) which flows to the NW at the base of the fault footwall, and the mapped surface rupture (thick black line).

method [31,32] finds minima in the misfit between observed and model displacements. To overcome the problem of local minima, we use a Monte-Carlo approach, starting the inversion 1000 times with randomly chosen starting parameters, the lowest minimum being retained as the final solution. The inversion determines ten parameters in all for the single dislocation solution — strike, dip, rake, slip, latitude and longitude, length of scarp, minimum and maximum depth, and a line-of-sight offset to allow for an incorrect assignment of the zero-displacement fringe.

In order to ensure that fault length L remains positive, and the depth of the top of fault and fault width remain within given bounds, the inversion procedure makes use of auxiliary parameters. For example, the length of the fault L is related to a parameter ρ by $L = e^{\rho}$. In the downhill simplex inversion, ρ is allowed values in the range $\pm\infty$ so that L is required to lie in the range $0 < L < \infty$. The depth of the top of the fault d is constrained to lie in the range $0 < d < d_{\max}$ by allowing the downhill simplex inversion to work with a parameter δ in the range $\pm\infty$, where

$$d = \frac{d_{\max}}{\pi}\left(\frac{\pi}{2} + \tan^{-1}\delta\right)$$

We assign a value of 25 km to $d_{\max}$ in order to loosely constrain the fault to lie within the seismo-

Table 3
Source parameters of the 1 October 1995 Dinar earthquake from inversion of SAR data

	Seismic [a]	Geodetic (1 segment)	Geodetic (4 segments)			
			1	2	3	4
Scarp latitude	38.09° [b]	38.132 ± 0.001°	38.172 ± 0.002°	38.143 ± 0.001°	38.114 ± 0.004°	38.085 ± 0.007°
Scarp longitude	30.17° [b]	30.117 ± 0.001°	30.078 ± 0.003°	30.103 ± 0.002°	30.129 ± 0.003°	30.155 ± 0.006°
Length (km)	–	11.4 ± 0.2	3.9 ± 0.35	3.9 ± 0.35	3.9 ± 0.35	3.9 ± 0.35
			Total Length = 15.6 ± 1.4			
M_0 (10^{18} N m)	3.1 ± 0.4	4.2 ± 0.1 [d]	1.36 ± 0.08	1.71 ± 0.09	0.94 ± 0.08	0.54 ± 0.13
			Total M_0 = 4.5 ± 0.1 [d]			
Slip (m)	–	1.41 ± 0.05	1.46 ± 0.08			
Strike	136°	148 ± 0.9°	145 ± 1.5°			
Dip	43°	53.8 ± 0.7°	49 ± 1°			
Rake	273°	277 ± 3°	270° (fixed)			
d_{min} (km)	4 [c]	2.1 ± 0.1	8.2 ± 0.6	1.4 ± 0.2	2.3 ± 0.2	3.8 ± 0.5
d_{max} (km)		8.2 ± 0.1	13.4 ± 0.5	8.0 ± 0.6	5.9 ± 0.2	5.9 ± 0.3
l.o.s. offset (mm) [e]	–	12 ± 1	−8 ± 4			

Fault segments are numbered starting at the NW, as in Fig. 6. Error bounds of 2σ are given for the geodetic parameters determined by inversion.
[a] From P- and SH-waveform modelling (this study).
[b] Location of surface scarp, projected up-dip from the centroid location.
[c] Depth to centroid; inferred depth range ~0–8 km, given that the fault broke the surface.
[d] Assuming Lamé elastic constants $\mu = 3.43 \times 10^{10}$ Pa, $\lambda = 3.22 \times 10^{10}$ Pa.
[e] The line-of-sight (l.o.s.) offset allows for the incorrect assignment of nominal zero fringe (e.g. if the fringe digitised with l.o.s. displacement −28 mm, was actually the zero displacement fringe, the inversion would yield a l.o.s. offset of −28 mm.).

genic upper crust. The vertical extent of the fault is constrained in a similar way. Apart from the length, depth and vertical extent of the fault, no constraint is placed on any of the parameters.

The source parameters obtained from our initial inversion of SAR fringes (Table 3) are used to create a model interferogram (Fig. 5a). The model explains the bulk of the deformation observed in the interferogram with the maximum displacement in approximately the same location and of the same magnitude, and fringes sub-parallel to the strike direction. The root-mean-square misfit (20 mm) corresponds to 2/3 of a fringe (1/3 of the radar wavelength). The surface projection of the fault plane we obtain by the inversion matches the surface observations of ground ruptures [8] except that the solution requires slip to continue for 3 km to the NW of the region of surface rupture and does not require any slip to be coincident with the SE angular segment of the fault. It is worth noting that the observed magnitude of slip [8] and the topographic expression of the fault (Fig. 2) are both smallest at the SE end, where there is no slip in this model. The geodetic moment for this single-fault model is $4.2 \pm 0.2 \times 10^{18}$ N m.

A-posteriori errors for individual parameters are determined using a Monte-Carlo simulation technique [32,33]. We determine 100 minimum-misfit solutions, each using the technique described above, except that the number of restarts can be reduced to 30 if the initial nodes of each simplex are constrained to be close to the best-fitting solution. The 100 solutions are obtained using different datasets, each one derived from the original with line-of-sight displacements randomly perturbed in a normal distribution about their original value using an a-priori standard deviation of 10 mm. The 2σ errors presented in Table 3 reflect the distribution of solutions found.

There is a good fit over the majority of the fringe pattern, but three areas in particular are not well modelled. Residual R_1 (Fig. 5b) arises from misfit between the maximum displacement in the model interferogram and the 'bull's eye' pattern of the real interferogram. The maximum in the calculated fringes is more elongate than the same feature in the real interferogram. A second significant residual (Fig. 5b, R_2) arises in the NW corner of the model interferogram where the model fringes do not have

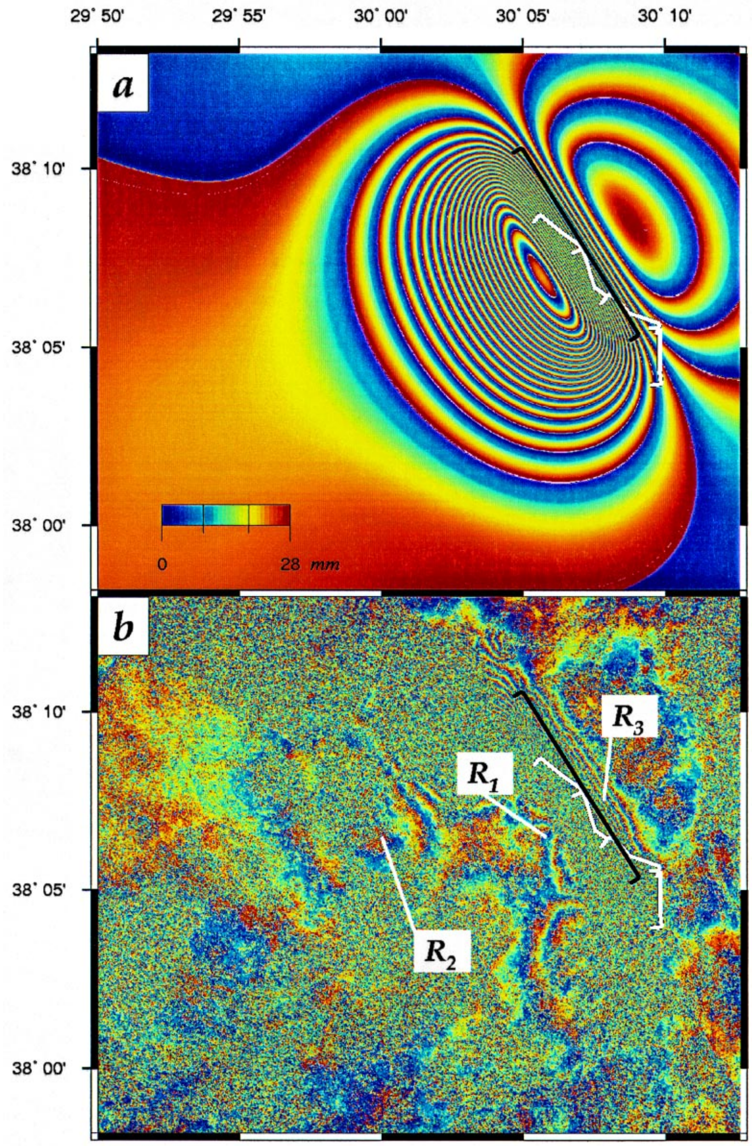

Fig. 5. (a) Model interferogram using a best-fit single fault model showing the location of the mapped surface rupture (white line) and the model fault plane (black line). (b) Residual interferogram, the result of subtracting the model interferogram from the real interferogram. R_1–R_3 denote the location of the largest systematic residuals using this model.

the observed tightness of curvature, the far-field pattern in our best-fit solution having smoother, more gradual changes. It is impossible to remove either of these residuals using our single fault model whilst maintaining a good fit to the remainder of the deformation pattern. In addition, we do not match the footwall fringes well with this simple model with several residual fringes running parallel to the model fault plane (Fig. 5b, R_3). These residual fringes are the result of a small amount of slip which reaches the surface; 25–30 cm of slip was observed at the surface in the field [8] but in our best-fit solution, slip stops 2 km subsurface. The solution estimates 1.4 m of slip on the fault, significantly larger than the 25–30 cm observed at the surface in the field [8]. The residual fringes in the footwall are probably the result of a discontinuity in the deformation at the surface rupture which is not included in the model.

Geological evidence [8] and variation in maximum line-of-sight displacement in the interferogram imply variable slip along the fault. To account for the misfits described above we introduce multiple fault segments of equal length, forced to lie on a single fault plane whose strike, dip, rake and location are solved for. There is a trade-off between depth range and slip for each segment such that if all other parameters are fixed, increasing the slip on the fault segment reduces the fault width without significantly increasing the misfit. Because of this, and to avoid overfitting the data, we only solve for a single value of slip applied to all segments.

In our single-fault solution we found a direct trade-off between the magnitude of slip on the fault and the rake. This trade-off occurs because the line of sight to the satellite is not far from vertical and, for rakes in the range of approximately 240º to 300º, the principal effect of a change in rake on calculated fringes is to alter their amplitude (in rough proportion to the vertical component of the slip vector) without greatly changing their spatial distribution. In consequence, the further from 270º the rake is, the larger is the slip required to fit the observed fringes. In order for our results not to be contaminated by this trade-off, we constrain the rake in our solution to be that found from seismological studies, namely 270º, which is the average of the Harvard CMT solution and our solution (Table 1).

Our best-fitting solution is generated from a four-segment inversion. Fifteen parameters are inverted for in all: strike, dip, slip, segment length and location applying to all segments (6), the vertical extent for each individual segment (8), and a line-of-sight offset of the fringes.

The inversion results (Table 3; Fig. 6) show an improved match to the observed interferogram, with all the major features of the original reproduced. The r.m.s. residual is reduced from 20 mm to 8 mm, or a quarter of a fringe, not significantly larger than levels of atmospheric noise observed in parts of the scene unaffected by the earthquake. Our solution implies that there are two separate areas of slip on the fault plane: a main rupture between depths of 1.4 and 8.0 km, the top of which deepens to the SE and matches the location of the observed surface rupture, and an along-strike continuation of the same fault plane, but between depths of 8.2 and 13.4 km and not associated with a surface rupture. We found that parameters on shallow segments are more tightly constrained than those on deeper segments. This is no surprise because small variations in shallow faulting have larger effects on surface displacements than the same variations on deeper segments.

The geodetic moment for this four-segment model is $4.5 \pm 0.1 \times 10^{18}$ N m. The 5-month time interval between SAR acquisitions means that our solution cannot give us information on the timing of slip in these different areas and hence we cannot definitively say that all of this moment was released during the mainshock. There were a number of secondary seismic events which occurred within a few days of the mainshock and may have contributed to the total geodetic moment. However, the largest aftershock had magnitude $M_{\mathrm{b}} = 5.0$ and is almost certainly too small to have a major influence on the total moment. It is impossible to quantify any additional contribution from post-seismic deformation.

The major region of misfit remains the footwall, again the result of the difference between our best-fit solution, which has about 1.4 m of slip that stops over 1 km below the surface, and the real situation, in which 25–30 cm of slip propagated to the surface. Atmospheric effects such as the altitude dependence of the propagation delay of electromagnetic waves in the lower troposphere [34] could also result in complications in the footwall fringe pattern, but these are unquantifiable without additional meteorological data. The misfit cannot be caused by an error in the DEM, because errors of over 1000 m would be required to produce a single fringe.

4. Source parameters from P- and SH-bodywave modelling

A number of published seismic mechanisms for the Dinar earthquake exist (Table 1), notably those determined from inversion of P-waves by Eyidŏgan and Barka [8] and Pinar [15]. These solutions differ from each other and from the Harvard CMT solution [16] whose seismic moment is more than twice as large. A source mechanism is sought using SH-bodywave inversion in addition to the P-waves

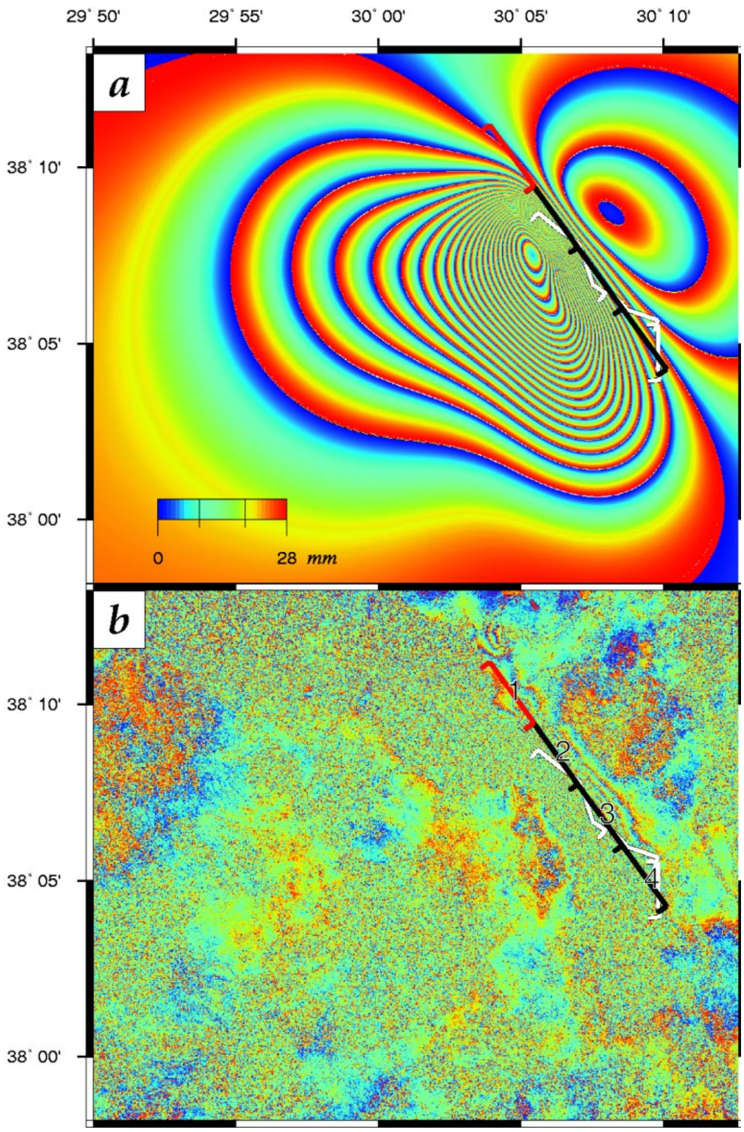

Fig. 6. (a) Model interferogram using a best-fit model, comprising three segments along the main rupture (black lines) and a deeper extension to the NW (red line). The location of the mapped surface rupture (white line) is shown for reference. (b) Residual interferogram, the result of subtracting the model interferogram from the real interferogram. Segment numbers correspond to those in Table 3.

used previously. The method and approach we use are described in detail elsewhere [35,36,2]. We use the MT5 software [39] to create a best-fit seismic inversion solution (Table 1, Fig. 7), using a half-space velocity model to calculate the synthetic seismograms, with $V_p = 6.0$ km s^{-1}, $V_s = 3.5$ km s^{-1} and density $= 2800$ kg m^{-3}, consistent with the geodetic modelling. The source time function is parameterised by overlapping isosceles triangles with 2 s half-width. The minimum misfit solution we obtain is quite robust, and converges to this solution from a variety of starting positions, including those of the Harvard CMT solution [16], Eyidŏgan and Barka [8], and Pinar [15].

Eyidŏgan and Barka [8], and Pinar [15] discount SH-waves because of noise levels. However, we

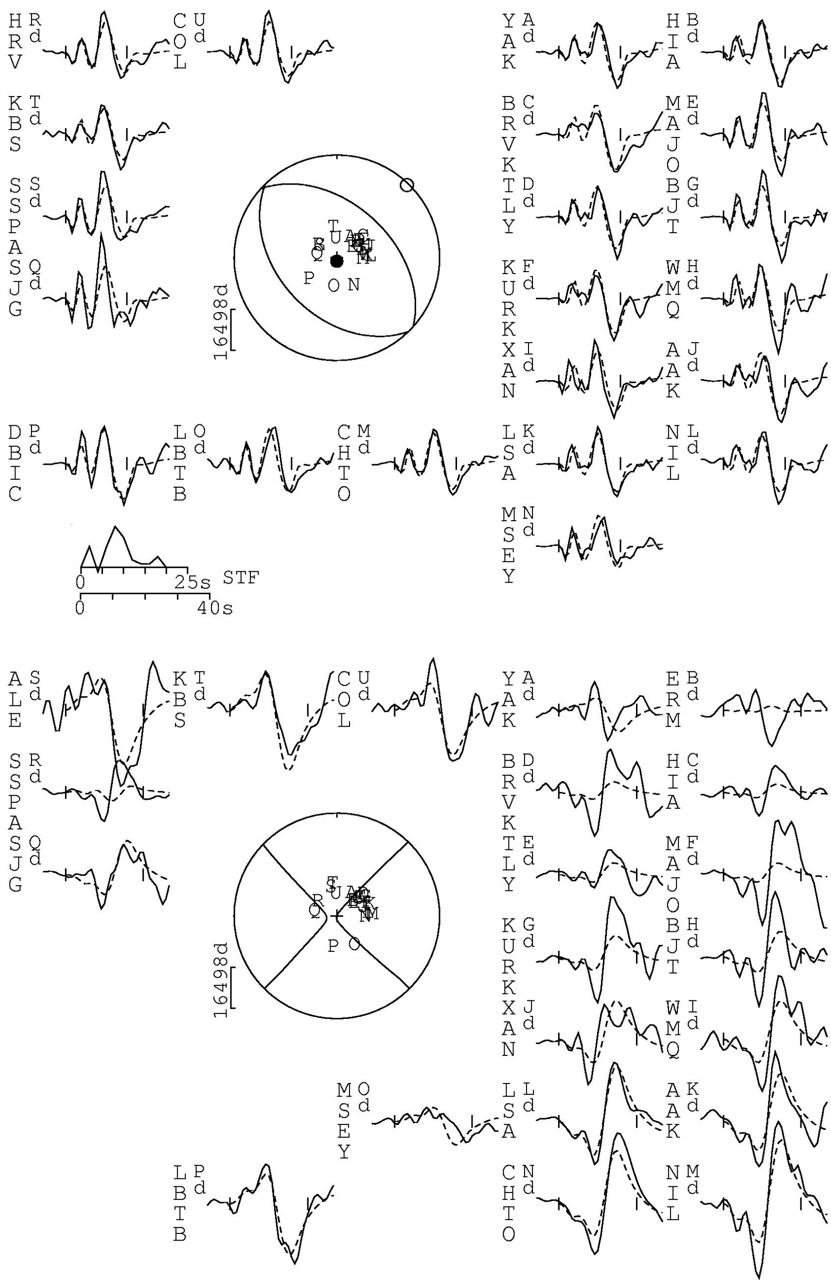

Fig. 7. P (top) and SH (bottom) observed (solid) and best-fitting synthetic (dashed) waveforms and focal spheres for the 1 October 1995 Dinar earthquake. Station positions on the focal spheres are identified by capital letters with waveforms arranged alphabetically and clockwise by azimuth according to their location on the focal sphere. *STF* is the source time function. Vertical ticks on the seismograms indicate the inversion window.

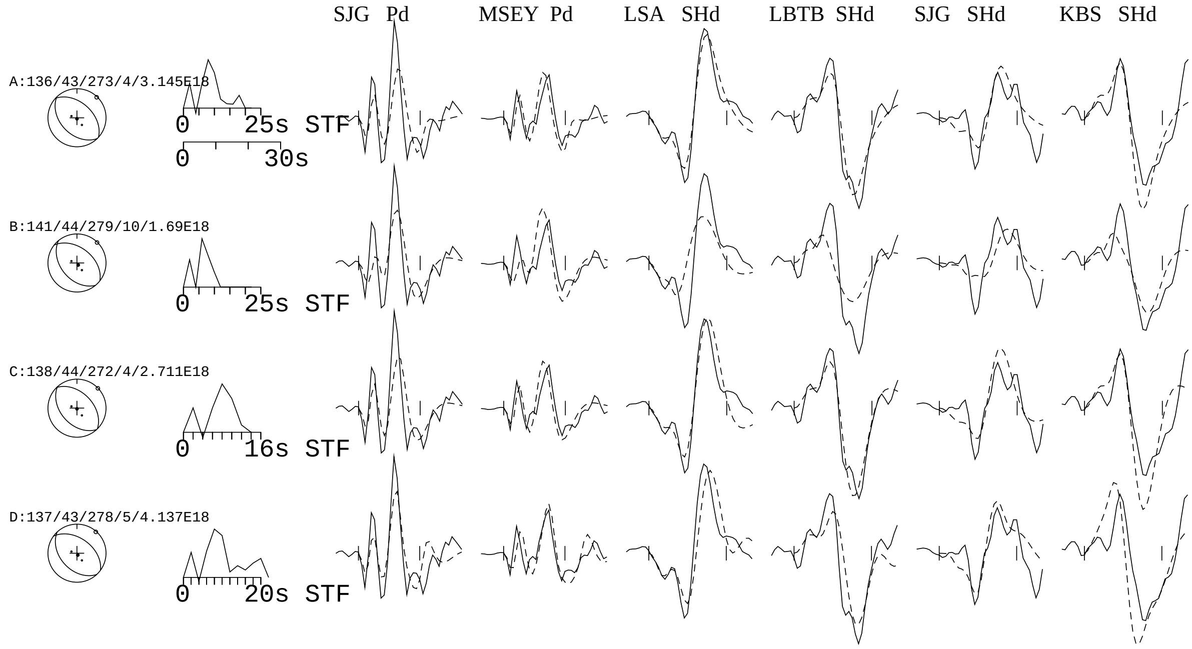

Fig. 8. Observed (solid) and synthetic (dashed) waveforms recorded at six different locations on the focal sphere. Vertical dashes indicate the length of the inversion window. (A) Best-fitting solution. (B) Solution with depth constrained to 10 km but with other parameters free. (C) Solution with source time function limited to 14 s duration, but all parameters free. (D) Solution with a source propagating NW (315º) at 2 km s^{-1} with all parameters free. Numbers above the P-wave focal sphere are strike/dip/rake/depth/M_0.

find numerous stations whose SH-waves are clear, with those at the same position on the focal sphere having very similar shapes (e.g. AAK, LSA, NIL, and CHTO; COL and KBS; SSPA and SJG), so we are confident these SH signals are robust. The fit to SH-waves is poor at a few stations very close to an SH nodal plane (e.g. ERM, HIA, BRVK) as in those cases the waveforms are extremely sensitive to very small changes in the nodal planes. At stations away from the nodal planes, and at a wide variety of azimuths, the fit to the SH-waveforms is good.

The principal feature of the source time function is a double pulse, corresponding to two bursts of moment release, or sub-events, with the larger second event starting about 5 s after the first. This is also a feature of the solutions of Eyidǒgan and Barka [8] and Pinar [15]. Our seismic moment is 80% larger than those determined from P-waves alone, although it is still smaller than the Harvard CMT solution [16]. The difference between the moment constrained by P-waveforms alone and that determined from both P- and SH-wave modelling probably arises because of a strong trade-off between the centroid depth and the length of the source time function, which leads to larger calculated seismic moments for events located at shallower depths [17]. Fig. 8 shows waveforms recorded at six stations from different parts of the focal sphere. Row A is our best-fitting solution, with a centroid depth of 4 km, and row B is the best-fitting solution with centroid depth constrained to 10 km, typical of the previously suggested depths. The deeper source is fit by a shorter source time function with a moment that is approximately half the size of the best fitting solution. Although the fit of the P-waves does not change greatly with increased depth, the SH-waves are modelled better by a shallow source thus requiring our moment to be larger than the published deeper sources.

The shape of the source time function (Fig. 8, row A) contains a tail at the end of the second (main) sub-event giving the time function a total duration of 20 s. If we limit the time function to 14 s duration, removing the tail, the resulting inversion (Fig. 8, row C) gives a solution whose fit to the waveforms is not significantly worse than in row A, and whose source parameters are also negligibly different except for the moment, which has been reduced from 3.1×10^{18} to 2.7×10^{18} N m. Thus about 10–15% of the moment in our best-fitting solution is contained in the tail of the time function, which is poorly resolved. This gives an informal indication of the likely error in the moment from this source, constraining the moment to $3.1 \pm 0.4 \times 10^{18}$ N m.

The published solutions from P-waves alone [8,15] indicate that the second sub-event is NW of the first, because the time delay between the two pulses in the P-waveforms apparently varies with azimuth. This conclusion critically depends on the onset time chosen for the P-waveforms: in our inversion this is fixed to the arrival time read on the (relatively) high-frequency broad-band records at all stations. If source directivity is significant, it will result in a compression of the time function and waveforms in the direction of rupture propagation and elongation of them in the opposite direction. There is a suggestion of such in the P-waveforms at some locations (e.g. MSEY and SJG). Tests using a source propagating NW (315º) at 2 km s^{-1} (Fig. 8, row D) improved the P-wave fit at several, but not all, stations, and the fit to the SH-waves worsens. We conclude that we cannot reliably resolve rupture propagation using the P and SH data.

Finally, Eyidǒgan and Barka [8] and Pinar [15] used the P-waves to suggest that the two pulses in the source time function had different orientations (Table 1). We did not find such variation necessary for modelling the P- and SH-waveforms, and the variation in orientation they suggest produced a very poor fit to the SH-waves. Nonetheless, a minor change in orientation of the second pulse could conceivably improve the fit to SH-waves at some nodal stations (e.g. ERM, HIA, BRVK).

The Harvard CMT solution [16], which differs in focal mechanism from the other solutions and has the largest moment obtained from seismic data, is also investigated. Test calculations holding centroid depth, strike, dip and rake fixed at the values in the Harvard CMT solution, with only source time function and moment free to vary, produce fits to the P- and SH-waves that are much poorer than those for the best-fitting solution. If the depth is also free to vary, the fits are improved but are still poorer than those for the solution obtained here. We note that the dip in the Harvard CMT catalogue solution is shallower than for most of the other solutions (Tables 1 and 3), suggesting that the larger moment may in part arise from the difficulty in resolving the M_{xz} and M_{yz} components of the moment tensor at long periods for shallow events [18,19]. Experiments in which these components are set to zero, corresponding to a dip of 45º, resulted in a reduction in moment of 15%, to 4.1×10^{18} N m (Table 1, G. Ekström, pers. commun.). In addition, the fixed centroid depth of 15 km used in the catalogue CMT solution is significantly deeper than the 4 km centroid depth determined from bodywave modelling and interferometry. If the centroid depth in the CMT inversion is fixed at 7 km in PREM (PREM assumes 3 km of water so this corresponds to a depth of 4 km into the solid earth) then the moment reduces further to 3.3×10^{18} N m (Table 1, G. Ekström, pers. commun.), close to the value that we determine from bodywave modelling.

5. Conclusions

Our best-fitting solution to the fringes from SAR interferometry consists of 1.4 m of slip on a fault striking 145º and dipping 49º and coinciding, for most of its length, with the extent of faulting indicated by mapped ground breaks [8]. In order to match the observed broadening of the fringes pattern to the NW (Fig. 3), it is necessary to include additional slip, between depths of 8.2 km and 13.4 km, on a NW prolongation of the fault plane.

The seismic solutions broadly agree, as to the strike and dip of the fault, with the interferometric solution (Tables 1 and 3). With the exception of the solution we present here, however, all the seismic solutions have significantly greater centroid depths than the centroid depth of 4–5 km that is required by the interferometric fringes. In our solution, the SH-data require a centroid depth of 4 km and hence (as discussed above) require a moment significantly greater ($3.1 \pm 0.4 \times 10^{18}$ N m) than those solutions [8,15] that are not constrained by SH-waves.

The moment obtained by Harvard CMT is greater still (4.7×10^{18} N m) than ours, though when that solution is constrained to have a dip of 45º and a depth of 4 km below solid ground (the standard depth of shallow CMT solutions is 15 km), the moment drops to 3.3×10^{18} N m (Table 1, G. Ekström, pers. commun.) in close agreement with the moment we determine from bodywave modelling, but 40% smaller than the geodetic moment ($4.5 \pm 0.1 \times 10^{18}$ N m). Note that, in constraining the rake in our geodetic solution to 270°, we have formed an estimate of the moment that is probably close to a minimum one. Solutions allowing the rake to vary yield moments of up to 5.4×10^{18} N m so there is little doubt that the seismic moment is much less than the geodetic moment. We do not know the reason for the discrepancy in moment estimates. A plausible source of this deformation is aseismic slip on the fault after the earthquake, as observed using GPS measurements after the Northridge and Loma-Prieta earthquakes [37,38], but we cannot test this without further data. It is also worth noting that the magnitude of the moment discrepancy corresponds to the magnitude of the moment on the deeper segment of our model which was not associated with a surface rupture.

A number of previous studies using a variety of geodetic techniques have found geodetic moments significantly larger than seismic moments, e.g. [29,33,40,41], but other studies have produced comparable moment estimates, e.g. [23,42–45]. The data are too few at present to draw any firm conclusions, but if seismology systematically underestimates the moment release associated with earthquakes then estimates of regional strain rate based on seismology, e.g. [13,14], may need revision.

Acknowledgements

We gratefully acknowledge the research studentship awarded to TJW by the Natural Environment Research Council in association with Nigel Press Associates. We thank Ren Capes, Geoff Lawrence and Nigel Press for encouraging us to undertake this study. We are grateful to Nigel Press Associates for providing ERS SAR and Landsat TM data, and for use of the PulSAR (SAR) and DERAin (interferometric) software. We also thank Andy Smith of Phoenix Systems for helpful discussions and support with this software, Paul Rosen and Scott Hensley of JPL for the use of their ROI_pac software, Göran Ekström for discussing with us his unpublished source modelling of the Dinar earthquake, and Keith Priestley for help in processing seismograms. Prompt reviews from Kurt Feigl, Alexis Rigo, Göran Ekström and an anonymous reviewer have improved the manuscript. Figures were prepared using the public domain GMT software [46]. ***[RO]***

References

[1] D. McKenzie, Active tectonics of the Alpine–Himalayan belt: the Aegean Sea and surrounding regions, Geophys. J.R. Astron. Soc. 55 (1978) 217–254.

[2] T. Taymaz, J. Jackson, D. McKenzie, Active tectonics of the north and central Aegean Sea, Geophys. J. Int. 106 (1991) 433–490.

[3] R. Reilinger, S.C. McClusky, M.B. Oral, R.W. King, M.N. Toksoz, A.A. Barka, I. Kinik, O. Lenk, I. Sanli, Global Positioning System measurements of present-day crustal movements in the Arabia–Africa–Eurasia plate collision zone, J. Geophys. Res. 102 (1997) 9983–9999.

[4] A. Barka, R. Reilinger, Active tectonics of the Eastern Mediterranean: deduced from GPS, neotectonic and seismicity data, Ann. Geofis. 40 (1997) 587–610.

[5] T. Taymaz, S. Price, The 1971 May 12 Burdur earthquake sequence, SW Turkey; a synthesis of seismological and geological observations, Geophys. J. Int. 108 (1992) 589–603.

[6] S. Price, B. Scott, Fault-block rotations at the edge of a zone of continental extension, southwest Turkey, J. Struct. Geol. 16 (3) (1994) 381–392.

[7] F. Şaroglu, Ö. Emre, İ. Kuşçu, Active Fault Map of Turkey, General Directorate of Mineral Research and Exploration (MTA), Eskişehir Yolu, 06520, Ankara, 1992.

[8] H. Eyidǒgan, A. Barka, The 1 October 1995 Dinar earthquake, SW Turkey, Terra Motae 8 (1996) 479–485.

[9] C.H. Scholz, A reappraisal of large earthquake faulting, Bull. Seismol. Soc. Am. 84 (1) (1994) 215–218.

[10] G. Pegler, S. Das, Analysis of the relationship between seismic moment and fault length for large crustal strike-slip earthquakes between 1977–92, Geophys. Res. Lett. 23 (9) (1996) 905–908.

[11] R. Davies, P. England, B. Parsons, H. Billiris, D. Paradissis, G. Veis, Geodetic strain of Greece in the interval 1892–1992, J. Geophys. Res. 102 (1997) 24571–24588.

[12] B. Kostrov, Seismic moment and energy of earthquakes and seismic flow of rock, Izv. Acad. Sci. USSR, Phys. Solid Earth 97 (1974) 23–44.

[13] J. Jackson, D. McKenzie, The relationship between plate motions and seismic moment tensors and the rate of active deformation in the Mediterranean and Middle East, Geophys. J.R. Astron. Soc. 93 (1988) 45–73.

[14] G. Ekström, P. England, Seismic strain rates in regions of distributed deformation, J. Geophys. Res. 94 (1989) 10231–10257.

[15] A. Pinar, Source inversion of the October 1, 1995, Dinar earthquake ($M_s = 6.1$): a rupture model with implica-

tions for seismotectonics in SW Turkey, Tectonophysics 292 (1998) 255–266.
[16] A.M. Dziewonski, G. Ekström, M.P. Salganik, Centroid-moment tensor solutions for October–December 1995, Phys. Earth Planet. Inter. 101 (1997) 1–12.
[17] J.A. Jackson, T. Blenkinsop, The Malaŵi earthquake of March 10, 1989: deep faulting within the East African Rift system, Tectonics 12 (1993) 1131–1139.
[18] H. Kanomori, J.W. Given, Use of long-period surface waves for fast determination of earthquake source parameters, Phys. Earth Planet. Inter. 27 (1981) 8–31.
[19] A.M. Dziewonski, J.H. Woodhouse, An experiment in systematic study of global seismicity: centroid-moment tensor solutions for 201 moderate and large earthquakes of 1981, J. Geophys. Res. 88 (1983) 3247–3271.
[20] D. Massonnet, M. Rossi, C. Carmona, F. Adragna, G. Peltzer, K. Fiegl, T. Rabaute, The displacement field of the Landers earthquake mapped by radar interferometry, Nature 364 (1993) 138–142.
[21] D. Massonnet, K.L. Feigl, Satellite radar interferometric map of the coseismic deformation field of the $M = 6.1$ Eureka Valley, California earthquake of May 17, 1993, Geophys. Res. Lett. 22 (12) (1995) 1541–1544.
[22] G. Peltzer, P. Rosen, Surface displacement of the 17 May 1993 Eureka Valley, California, earthquake observed by SAR interferometry, Science 268 (1995) 1333–1336.
[23] B. Meyer, R. Armijo, J.B. de Chabalier, C. Delacourt, J.C. Ruegg, J. Acache, P. Briole, D. Papanastassiou, The 1995 Grevena (northern Greece) earthquake: fault model constrained with tectonic observations and SAR interferometry, Geophys. Res. Lett. 23 (19) (1996) 2677–2680.
[24] B. Hernandez, F. Cotton, M. Campillo, D. Massonnet, A Comparison between short term (co-seismic) and long term (one year) slip for the Landers earthquake: measurements from strong motion and SAR interferometry, Geophys. Res. Lett. 22 (18) (1995) 2517–2520.
[25] D. Massonnet, K.L. Feigl, Radar interferometry and its application to changes in the earth's surface, Rev. Geophys. 36 (1998) 441–500.
[26] R.M. Goldstein, H.A. Zebker, C.L. Werner, Satellite radar interferometry: two-dimensional phase unwrapping, Radio Sci. 23 (4) (1988) 713–720.
[27] H.A. Zebker, C. Werner, P.A. Rosen, S. Hensley, Accuracy of topographic maps derived from ERS-1 interferometric radar, IEEE Trans. Geosci. Remote Sensing 32 (4) (1994) 823–836.
[28] Y. Okada, Surface deformation due to shear and tensile faults in a half-space, Bull. Seismol. Soc. Am. 75 (4) (1985) 1135–1154.
[29] P.J. Clarke, D. Paradissis, P. Briole, P.C. England, B.E. Parsons, H. Billiris, G. Veis, J.-C. Ruegg, Geodetic investigation of the 13 May 1995 Kozani–Grevena (Greece) earthquake, Geophys. Res. Lett. 24 (6) (1997) 707–710.
[30] P.J. Clarke, Tectonic Motions and Earthquake Deformation in Greece from GPS Measurements, D.Philos. thesis, University of Oxford, 1996, 274 pp.
[31] J.A. Nelder, R. Mead, A simplex method for function minimisation, Comput. J. 7 (1965) 308–313.
[32] W.H. Press, S.A. Teukolsky, W.T. Vetterling, B.P. Flannery, Numerical Recipes in C: The Art of Scientific Computing, 2nd ed., Cambridge University Press, Cambridge, 1992, 994 pp.
[33] K.L. Feigl, A. Sergent, D. Jacq, Estimation of an earthquake focal mechanism from a satellite radar interferogram; application to the December 4, 1992 Landers aftershock, Geophys. Res. Lett. 22 (9) (1995) 1037–1040.
[34] C. Delacourt, P. Briole, J. Achache, Tropospheric corrections of SAR interferograms with strong topography; application to Etna, Geophys. Res. Lett. 25 (15) (1998) 2849–2852.
[35] J. Nabelek, Geometry and mechanism of faulting of the 1980 El Asnam, Algeria, earthquake from inversion of teleseismic body waves and comparison with field observations, J. Geophys. Res. 90 (1985) 12713–12728.
[36] R. McCaffrey, J. Nabelek, Earthquakes, gravity and the origin of the Bali basin: and example of a nascent continental fold-and-thrust belt, J. Geophys. Res. 92 (1987) 441–460.
[37] A. Donnellan, G. Lyzenga, GPS observations of fault afterslip and upper crustal deformation following the Northridge earthquake, J. Geophys. Res. 103 (1998) 21285–21297.
[38] F. Pollitz, R. Burgmann, P. Segall, Joint estimation of afterslip rate and postseismic relaxation following the 1989 Loma Prieta earthquake, J. Geophys. Res. 103 (1998) 26975–26992.
[39] P. Zwick, R. McCaffrey, G. Abers, MT5 Program, IASPEI Software Library 4, 1995.
[40] J. Dvorak, An Earthquake cycle along the south flank of Kilauea volcano, Hawaii, J. Geophys. Res. 99 (1994) 9533–9541.
[41] J. Ruegg, J. Campos, R. Armijo, S. Barrientos, P. Briole, R. Thiele, M. Arancibia, J. Canuta, T. Duquesnoy, M. Chang, D. Lazo, H. Lyon-Caen, L. Ortlieb, J. Rossignol, L. Serrurier, The $M(\mathrm{W}) = 8.1$ Antofagasta (North Chile) earthquake of July 30, 1995: first results from teleseismic and geodetic data, Geophys. Res. Lett. 23 (9) (1996) 917–920.
[42] J. Campos, R. Madariaga, C. Scholz, Faulting process of the August 8, 1993, Guam earthquake: a thrust event in an otherwise weakly coupled subduction zone, J. Geophys. Res. 101 (1996) 17581–17596.
[43] J. Freymueller, N. King, P. Segall, The coseismic slip distribution of the Landers earthquake, Bull. Seismol. Soc. Am. 84 (1994) 646–659.
[44] S. Larsen, R. Reilinger, H. Neugebauer, W. Strange, Global Positioning System measurements of deformations associated with the 1987 Superstition Hills earthquake — evidence for conjugate faulting, J. Geophys. Res. 97 (1992) 4885–4902.
[45] C. Williams, T. Arnadottir, P. Segall, Coseismic deformation and dislocation models of the 1989 Loma-Prieta earthquake derived from Global Positioning System measurements, J. Geophys. Res. 98 (1993) 4567–4578.
[46] P. Wessel, W.H.F. Smith, New, improved version of Generic Mapping Tools released, Eos 79 (1998) 579.